Electronic Supplementary Material (ESI) for Journal of Materials Chemistry A.

Supporting Information

Single crystal derived precursor for improving performance of $CsSnI_3$ perovskite solar cells

Qiang Sun [a, ‡], Anjie Gu [a, ‡], Haixuan Yu [a], Yan Shen [a] and Mingkui Wang*[a]

[a] Wuhan National Laboratory for Optoelectronics, Huazhong University of Science and Technology, 1037 Luoyu Road, Wuhan 430074, Hubei, P. R. China.

‡ These authors contributed equally to this work.

*Corresponding author: mingkui.wang@mail.hust.edu.cn

Material and methods

Material:

CsI (99.99%, Sigma Aldrich), SnI_2 (99.99%, Sigma Aldrich), N, N-Dimethylformamide (DMF, Anhydrous 99.8%, Sigma Aldrich), dimethyl sulfoxide (DMSO, Anhydrous ≥99.5%, Sigma Aldrich), [6,6]-Phenyl C61 butyric acid methyl ester (PCBM, >99.5%, Sigma Aldrich) were used as received without further purification. Poly(3,4-ethylenedioxythiophene) polystyrene sulfonate (PEDOT:PSS) and Bathocuproine (BCP) were purchased from Xi'an p-OLED.

PSC devices fabrication:

ITO glasses were sequentially cleaned in detergent, deionized water, acetone, isopropanol, and alcohol for 20 minutes. Afterward, the glasses were treated with ultraviolet ozone for 30 minutes. PEDOT: PSS films were coated on the cleaned ITO-glasses at 4500 rpm for 40 s and then annealed in air at 145 °C for 20 min. The perovskite film was deposited onto the substrate using a warm (50-60 °C) perovskite precursor solution in the N_2-filled glovebox. The mixture of CsI and SnI_2 (with a molar ratio of 1: 1) or $CsSnI_3$ single crystals were dissolved in the mixed solvent of DMF and DMSO (v/v, 9:1) to obtain a 0.8 M solution. The S-$CsSnI_3$ and/or C-$CsSnI_3$ films were coated on the HTL by spin-coating the precursor solution at 3000 rpm for 30s. All of the deposited perovskite films were rested for 30 min prior to annealing. The substrates were further annealed at 80 °C for 10 min. The PCBM solution was prepared by dissolving 20 mg PCBM in 1 mL chlorobenzene. 50 μL of the PCBM solution was then dropped onto the perovskite films and spin-coated at 2000 rpm for 30 s. A 0.5 mg mL^{-1} BCP/anhydrous isopropanol solution was spin-coated at 6000 rpm for 30 s, followed by annealing at 60 °C for 10 min. Finally, a 100 nm Ag electrode was deposited using a thermal evaporator to finish the device fabrication.

Characterization:

Single-crystal X-ray diffraction (SCXRD) was measured using XtaLAB PRO MM007HF Cu. X-ray diffraction (XRD) experiments were conducted using a Philips

X-ray diffractometer with Cu Kα radiation to measure the crystal structure. The film light absorption was measured with a PE950 spectrophotometer at room temperature. The film morphology was obtained with a field-emission scanning electron microscope (FEI Nova Nano SEM 450). The steady-state photoluminescence (PL) spectrum was measured by a fluorescence spectrophotometer (LabRAM HR800). Inductively coupled plasma optical emission spectroscopy (ICP-OES) was measured using Prodigy Plus ICP-OES. X-ray photoelectron spectrometer (XPS) measurements were conducted on an AXIS SUPRA system (Kratos Analytical Ltd.). Time-resolved photoluminescence decays (TRPL) were measured by Delta Flex Fluorescence Lifetime System (Horiba Scientific Com., Japan). The photocurrent density-voltage (J-V) characteristics of the devices were obtained by applying an external potential bias to the devices and measuring the generated photocurrent with a Keithley model 2400 digital source meter.

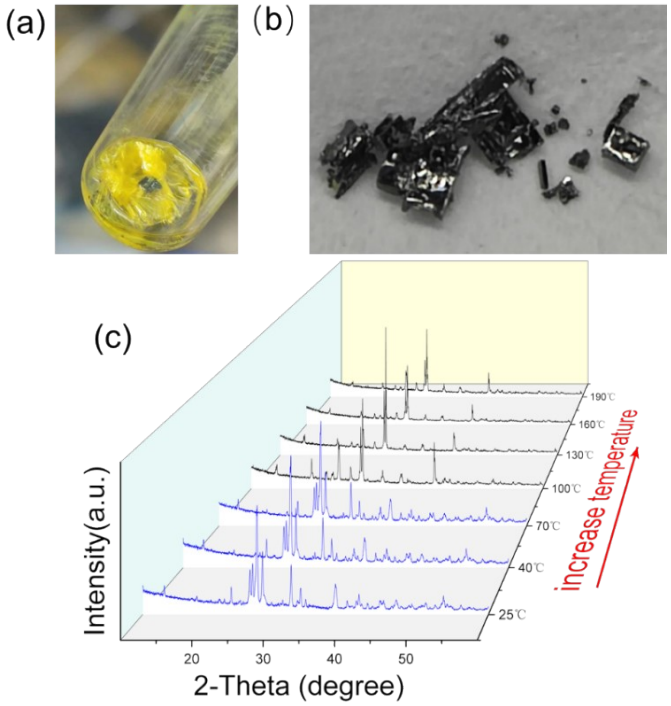

Figure S1. The optical images of (a) the yellow needle-like crystals and (b) the black bulk crystals. (c) XRD patterns of the crystals prepared at different temperatures, where the blue lines represent the formation of the Y-$CsSnI_3$ phase, black lines represent the formation of B-γ $CsSnI_3$ phase.

At room temperature, this material exists in two polymorphs: the edge-connected 1D double-chain structure (Y-$CsSnI_3$, Figure S1a), which is a non-photoactive phase and the corner-linked 3D perovskite structure (B-γ $CsSnI_3$, Figure S1b), which is a desirable photoactive phase. Further, we examined the crystal phases grown at a series of temperatures and determined that 100°C is the lowest temperature for the B-γ $CsSnI_3$ preparation through this method (Figure S1c).

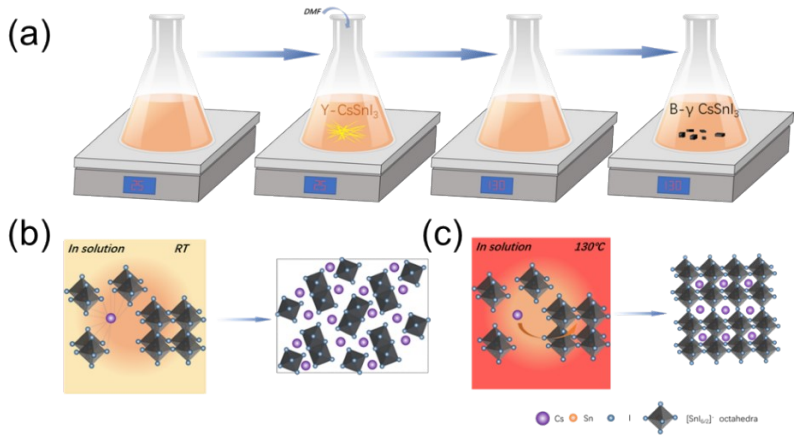

Figure S2. (a) Schematic diagram of the synthesis pathways of phase pure Y-$CsSnI_3$ and B-γ $CsSnI_3$ single crystals. Crystal growth mechanism of (b) the Y-$CsSnI_3$ and (c) the B-γ $CsSnI_3$ crystal structure in the precursor.

The precursors were crystallized once at room temperature and once at 130 °C (Figure S2a). The yellow phase was obtained at room temperature, whose crystal structure was Cs ions surrounded by three adjacent $Sn_2I_6^{2-}$ chains (Figure S2b). In contrast, the black phase was obtained at 130 ℃, and its crystal structure was a three-dimensional network structure of $[SnI_{6/2}]$-octahedra stacked by angle sharing, while Cs ions filled into the interstitial positions constructed by the octahedra, constituting a three-dimensional chalcogenide structure (Fig. S2C). It has been reported in the literature that Cs atoms play a key role in determining the phase structure of $CsSnI_3$.[1] Therefore, this phenomenon of forming different single-crystal structures at different temperatures may be attributed to the following: while at lower temperatures the Cs ions have difficulty crossing the energy barrier into the octahedral gap position and eventually fail to form the perovskite phase; When the solution temperature reaches 130°C, the temperature intensifies the molecular thermal motion of the Cs ions in solution, providing sufficient activation energy to drive the Cs ions into the $[SnI_{6/2}]$-octahedral gap position to form a perovskite structure.

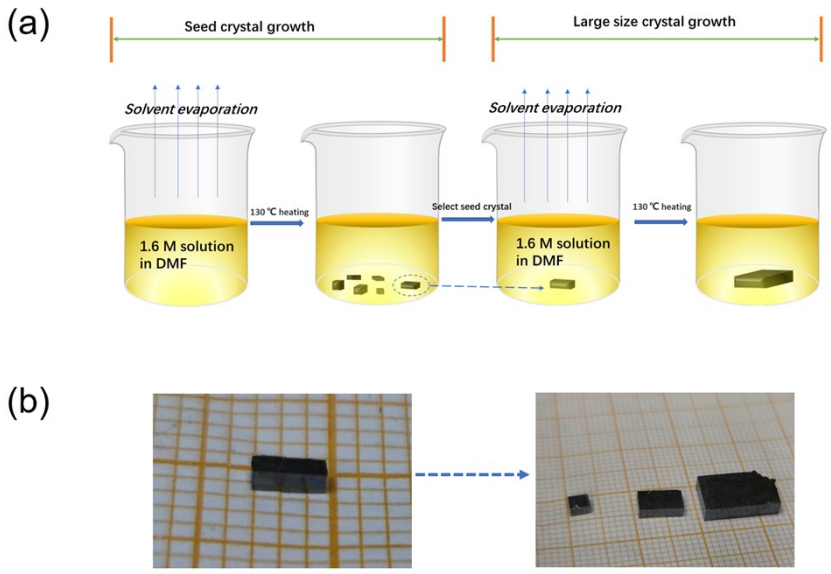

Figure S3. (a) Growth method of large-sized single crystals. (b) Optical image of large B-γ $CsSnI_3$ single crystals (each cell represents 1mm).

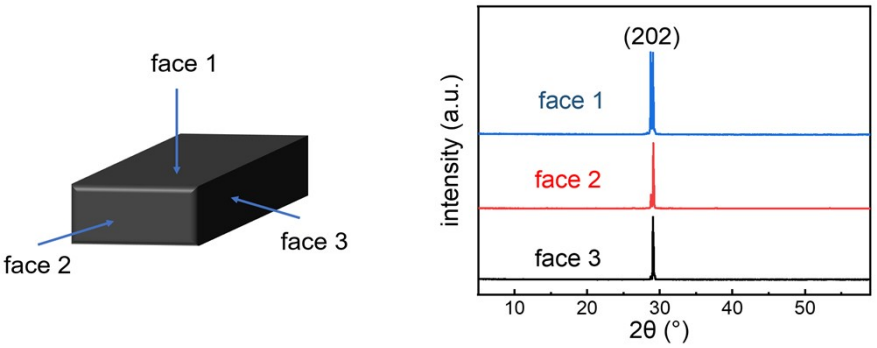

Figure S4. (a) XRD of the three exposed surfaces of the $CsSnI_3$ single crystal.

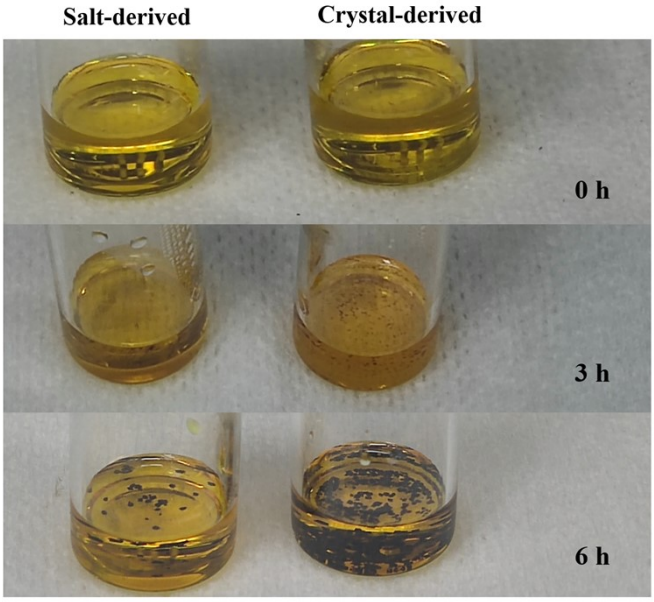

Figure S5. Time-varying crystallization products of $CsSnI_3$ in salt-derived precursor solution (left) and crystal-derived precursor solution (right).

We carefully compared nucleation processes of $CsSnI_3$ in salt-derived precursor solution (left) and crystal-derived precursor solution (right). After 3 h, the colors of these two solutions both deepened from pale yellow to light golden, indicating the solutions were mostly saturated, and nucleation begins in the crystals-derived precursor solution. After 6 h, a mass of the $CsSnI_3$ crystal nucleus were precipitated from the crystals-derived precursor solution while only bits of $CsSnI_3$ crystal nucleus precipitated from the salt-derived precursor solution.

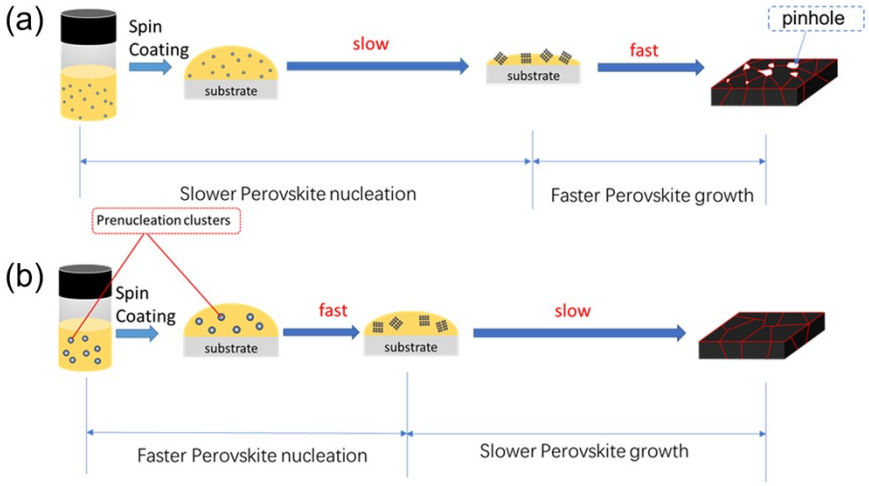

Figure S6. Schematic diagram of crystal nucleation and growth processes in (a) salt-derived precursor solution and (b) crystal-derived precursor solution.

To better understand the crystal nucleation and growth processes of the two different precursor solutions on PEDOT: PSS substrates. We drew a schematic diagram of the effect of pre-nucleation in the formation process of B-γ $CsSnI_3$ films (Figures S6). The salt-derived precursor solution has a lower nucleation rate, and when nuclei are formed, there is a severe shortage of solution available for crystal growth, which then leads to numerous pinholes in the film. In contrast, a relatively high nucleation rate in crystal-derived precursor solution could balance the rate of crystal nucleation and growth, and finally form a uniform, dense, and pinhole-free $CsSnI_3$ thin film.

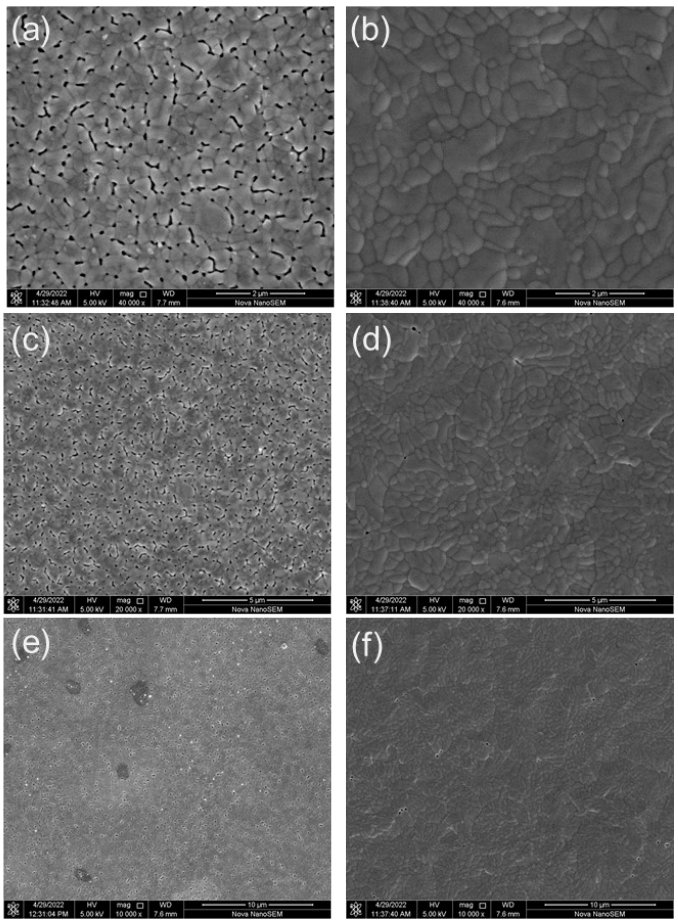

Figure S7. SEM images of the S-$CsSnI_3$ and C-$CsSnI_3$ films at various magnifications.

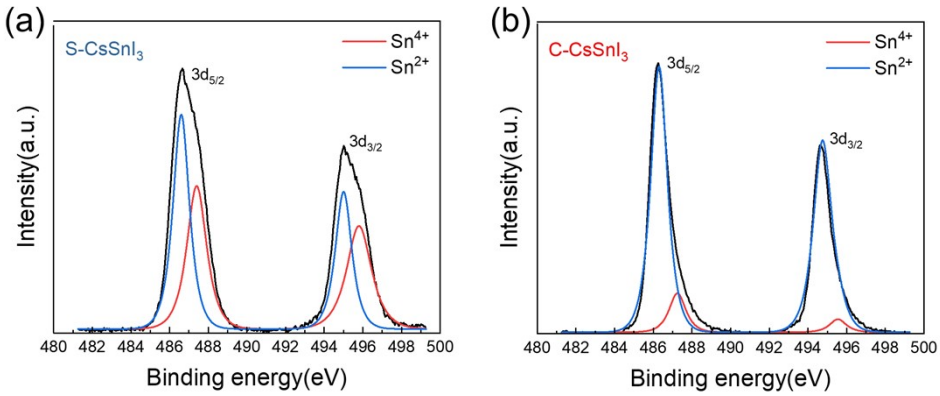

Figure S8. XPS characterization of (a) the S-$CsSnI_3$ and (b) C-$CsSnI_3$ thin films after 24 hours of aging in ambient air (25˚C with 30% relative humidity).

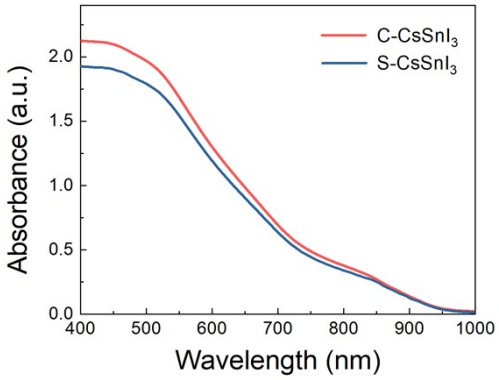

Figure S9. UV-visible absorption spectroscopy characterization of the S-$CsSnI_3$ and C-$CsSnI_3$ films.

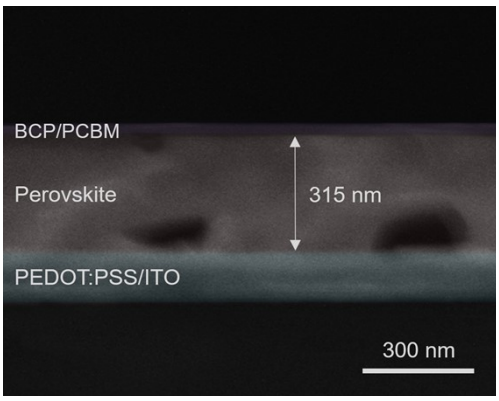

Figure S10. Cross-sectional SEM image of the S-$CsSnI_3$ based device.

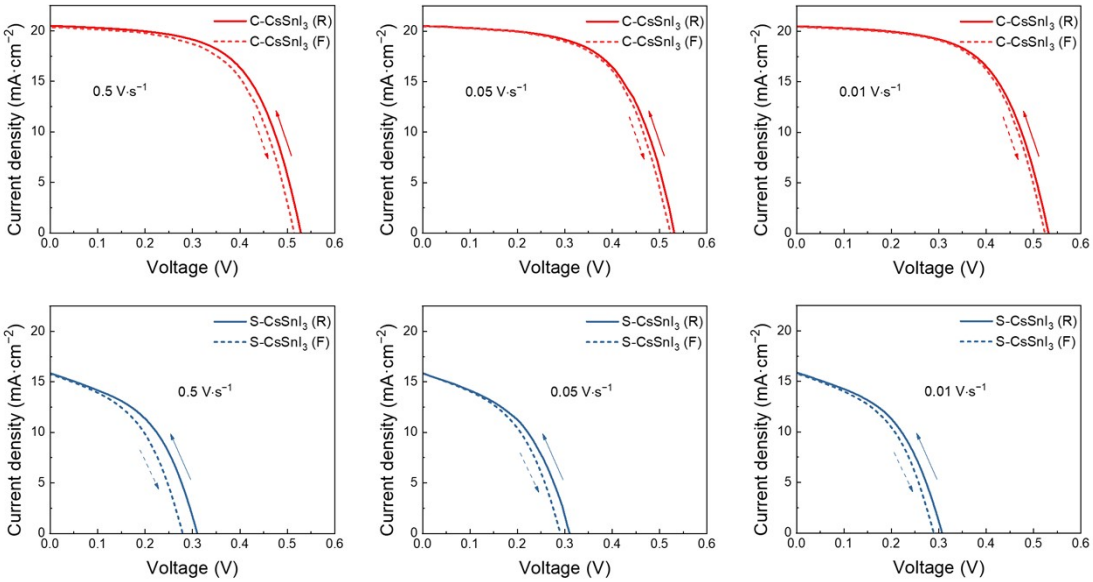

Figure S11. *J-V* measurements of the C-$CsSnI_3$ and S-$CsSnI_3$ based PSCs with different scan rates in both reverse and forward scan direction.

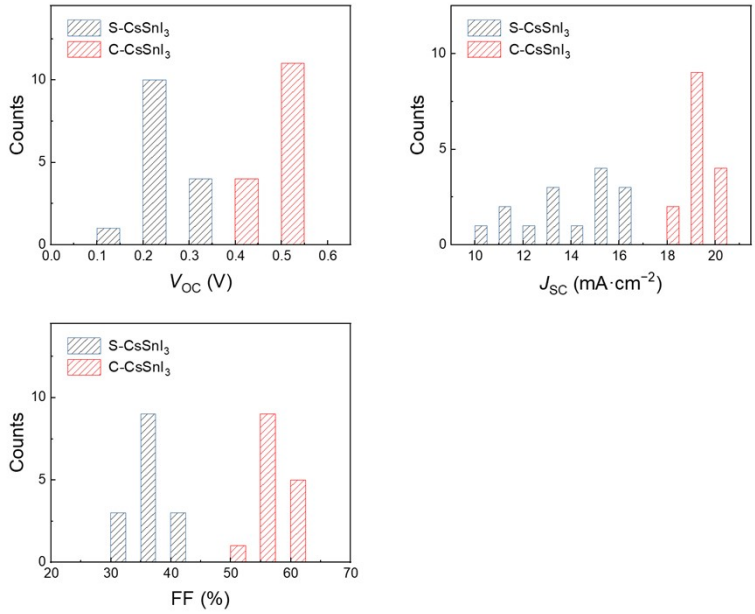

Figure S12. V_{OC}, J_{SC} and FF distribution of the C-$CsSnI_3$ and S-$CsSnI_3$ based PSCs obtained from current density-voltage measurements.

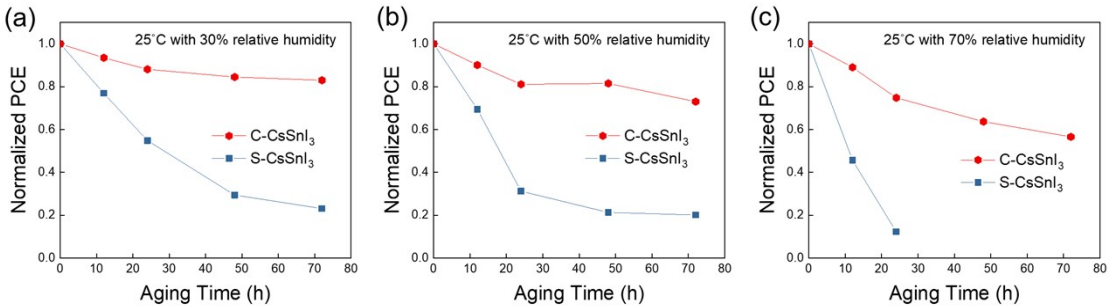

Figure S13. Stability tests of the unencapsulated PSCs under different relative humidity conditions.

Table S1. Analytical parameters of the B-γ $CsSnI_3$ single crystal.

Table 1 Crystal data and structure refinement for CsSnI3	
Identification code	CsSnI3
Empirical formula	CsSnI3
Formula weight	421.53
Temperature/K	293.2(2)
Crystal system	orthorhombic
Space group	Pnma
a/Å	8.6944(5)
b/Å	12.3862(7)
c/Å	8.6562(9)
α/°	90
β/°	90
γ/°	90
Volume/Å3	932.19(12)
Z	1
ρcalcg/cm3	0.751
μ/mm-1	19.295
F(000)	180.0
Crystal size/mm3	0.12 × 0.07 × 0.05
Radiation	CuKα (λ = 1.54184)
2Θ range for data collection/°	12.476 to 147.644
Index ranges	-10 ≤ h ≤ 10, -15 ≤ k ≤ 15, -7 ≤ l ≤ 9
Reflections collected	5170
Independent reflections	867 [Rint = 0.1273, Rsigma = 0.0762]
Data/restraints/parameters	867/0/28
Goodness-of-fit on F2	1.653
Final R indexes [I>=2σ (I)]	R1 = 0.1282, wR2 = 0.3967
Final R indexes [all data]	R1 = 0.1358, wR2 = 0.4023
Largest diff. peak/hole / e Å-3	5.98/-2.93

Table S2. Fitting parameters of PL decay lifetime of the C-$CsSnI_3$ and S-$CsSnI_3$ films.

	τ_1 (ns)	A_1	τ_2 (ns)	A_2	$\tau_{average}$ (ns)
S-$CsSnI_3$	0.19	76.7	7.22	23.3	1.83 ns
C-$CsSnI_3$	0.43	61.3	13.87	38.7	5.63 ns

Table S3. Photovoltaic parameters of the optimized C-$CsSnI_3$ and S-$CsSnI_3$ PSCs.

	V_{OC} (V)	J_{SC} (mA cm^{-2})	FF (%)	PCE (%)
S-CsSnI3	0.31	15.84	46.1	2.26
C-CsSnI3	0.53	20.50	60.1	6.53

Table S4. Photovoltaic parameters and hysteresis index data of the C-$CsSnI_3$ and S-$CsSnI_3$ based PSCs with different scan rates.

	Scan rate	Scan direction	V_{OC} (V)	J_{SC} (mA cm^{-2})	FF (%)	PCE (%)	Hysteresis index
C-$CsSnI_3$	0.5 mV s^{-1}	Reverse	0.53	20.49	60.4	6.56	1.9
		Forward	0.51	20.34	60.1	6.23	
	0.05 mV s^{-1}	Reverse	0.53	20.50	60.1	6.53	1.3
		Forward	0.52	20.46	60.9	6.48	
	0.01 mV s^{-1}	Reverse	0.53	20.48	60.2	6.53	0.9
		Forward	0.52	20.44	61.1	6.50	
S-$CsSnI_3$	0.5 mV s^{-1}	Reverse	0.31	15.83	46.3	2.28	6.3
		Forward	0.28	15.75	45.5	2.01	
	0.05 mV s^{-1}	Reverse	0.31	15.84	46.1	2.26	3.8
		Forward	0.29	15.80	45.6	2.09	
	0.01 mV s^{-1}	Reverse	0.31	15.83	46.0	2.26	3.1
		Forward	0.29	15.77	46.0	2.10	

The hysteresis index (HI) of the devices were calculated by the following equation:

$HI = [J_{RS}(0.8V_{OC}) - J_{FS}(0.8V_{OC})]/J_{RS}(0.8V_{OC})$

Where $J_{RS}(0.8V_{OC})$ and $J_{FS}(0.8V_{OC})$ on behalf of the J_{SC} at 80% of V_{OC} for the reverse scan and forward scan, respectively.

Table S5. Photovoltaic parameters of the S-$CsSnI_3$ based PSCs.

	V_{OC} (V)	J_{SC} (mA cm^{-2})	FF (%)	PCE (%)
1	0.30	13.96	45.8	1.92
2	0.29	14.96	42.8	1.86
3	0.19	12.36	38.1	0.89
4	0.31	15.74	41.1	2.01
5	0.30	16.31	41.5	1.94
6	0.29	16.453	44.6	2.13
7	0.26	15.67	43.9	1.79
8	0.28	16.92	45.2	2.14
9	0.20	11.24	38.6	0.87
10	0.23	10.36	41.1	0.98
11	0.21	11.23	39.6	0.93
12	0.24	13.21	40.2	1.27
13	0.28	15.68	43.6	1.91
14	0.23	13.53	42.9	1.34
15	0.31	15.84	46.1	2.26

Table S6. Photovoltaic parameters of the C-$CsSnI_3$ based PSCs.

	V_{OC} (V)	J_{SC} (mA cm^{-2})	FF (%)	PCE (%)
1	0.52	20.09	60.7	6.34
2	0.51	19.92	62.1	6.31
3	0.49	19.43	55.8	5.31
4	0.53	20.50	60.1	6.53
5	0.52	19.14	61.2	6.09
6	0.51	19.86	56.9	5.76
7	0.47	18.84	54.5	4.83
8	0.50	20.21	59.2	5.98
9	0.44	19.32	58.2	4.95
10	0.49	19.36	55.2	5.24
11	0.54	19.66	59.2	6.28
12	0.53	19.14	60.2	6.11
13	0.51	18.80	58.4	5.60
14	0.50	19.83	59.9	5.94
15	0.51	20.55	57.8	6.06

References

1. I. Chung, J. Song, J. Im, J. Androulakis, C. Malliakas, H. Li, A. Freeman, J. Kenney and M. Kanatzidis, J. Am. Chem. Soc., 2012, 134, 8579–8587.